INTERNATIONAL JOURNAL OF HYDROGEN ENERGY 36 (2011) 6510–6518

Available at www.sciencedirect.com

ScienceDirect

journal homepage: www.elsevier.com/locate/he

The reactor design for photoelectrochemical hydrogen production

Chung-Jen Tseng*, Chia-Lin Tseng

Department of Mechanical Engineering, National Central University, No. 300, Jhongda Road, Chungli 32001, Taiwan, ROC

ARTICLE INFO

Article history:
Received 26 August 2010
Received in revised form
1 March 2011
Accepted 7 March 2011
Available online 3 April 2011

Keywords:
Solar hydrogen production
Photoelectrochemical method
Reactor design

ABSTRACT

The heat transfer and flow characteristics of a photoelectrochemical (PEC) hydrogen generation reactor are investigated numerically. Four different reactor designs are considered in this study. The solar irradiation is separated into short and long wavelength parts depending on the energy band gap of the photoelectrode used. While short wavelength part is used to generate electron and hole pairs, the long wavelength part is used to heat the system. Because the energy required for splitting water decreases as temperature is increased, heating the reactor by using the long wave energy increases the system efficiency. Thus, how the long wavelength energy is absorbed by the reactor is very important.

The results show that more long wavelength energy kept inside the reactor can increase the solar-to-hydrogen efficiency, η_{SH}. For Fe_2O_3 photoelectrode, careful reactor design can increase η_{SH} by 11.0%. For design D under 4000 W/m^2 irradiation and a quantum efficiency of 30%, η_{SH} is found to be 14.1% and the hydrogen volume production rate is 166 L/m^2 h for Fe_2O_3. Effects of several parameters on the PEC hydrogen reactor are also discussed.

1. Introduction

Hydrogen is regarded as a potential energy carrier for the future. There exist several methods to produce hydrogen from various sources. One promising method is photoelectrochemical (PEC) decomposition of water into hydrogen and oxygen. Both the reactant of water and the energy source from the sun are readily available, renewable, and environmentally clean. Since Fujishima and Honda [1] proved that water can be effectively split into its constituents on a photoelectrode covered with n-type TiO_2 semiconductor, considerable attention has been devoted to the photodecomposition of water as an alternative solar energy conversion process leading to a non-polluting fuel [2–5].

A PEC cell consists of a semiconductor electrode and a metal counter electrode immersed in an aqueous electrolyte. As light is incident on the semiconductor, it absorbs part of the light and generates electron and hole pairs. These electron and hole pairs react with water and split it into hydrogen and oxygen.

The process can be summarized in the following equations [6,7]:

$$\text{Solar}: 2h\nu \rightarrow 2e^- + 2h^+ \tag{1}$$

$$\text{Anode}: 2h^+ + H_2O_{(l)} \rightarrow \frac{1}{2}O_{2(g)} + 2H^+_{(aq)} \tag{2}$$

$$\text{Cathode}: 2e^- + 2H^+_{(aq)} \rightarrow H_{2(g)} \tag{3}$$

$$\text{Overall}: 2h\nu + H_2O_{(l)} \rightarrow \frac{1}{2}O_{2(g)} + H_{2(g)} \tag{4}$$

Licht [8–10] recently proposed a model to increase the hydrogen production efficiency. While the high frequency solar irradiation is used for photo-electronic conversion, the low frequency sub-band-gap part is used for heating the electrolyte solution to lower the water-splitting potential. This provides a process of efficient water splitting by using the solar energy.

* *Corresponding author*. Tel.: +886 34267348; fax: +886 34254501.
E-mail address: cjtseng@ncu.edu.tw (C.-J. Tseng).
0360-3199/$ – see front matter
doi:10.1016/j.ijhydene.2011.03.025

Nomenclature

A	thickness of insulator
C_p	specific heat
E_g	energy band gap
E_s	energy available for splitting water
E_{in}	total solar incident energy
E_λ	spectral solar energy
g	gravity
G	thickness of glass
ΔG_{H_2O}	Gibbs free energy of water dissociation reaction
ΔH_{H_2}	heating value of hydrogen
H^+	proton
h^+	electron hole
h	Planck's constant $= 6.626 \times 10^{-34}$ J
e^-	electron
I_λ	spectral radiative intensity
$I_{b\lambda}$	black body spectral radiative intensity
k	thermal conductivity
k_A	thermal conductivity of insulator
QE	quantum efficiency
T	temperature
W	distance between anode and glass wall
α_{ave}	average absorption coefficient
α_λ	spectral absorption coefficient
β	thermal expansion coefficient
η_{SH}	solar–to-hydrogen conversion efficiency
λ	wavelength
υ	frequency
ϕ	hydrogen volume production rate

Grzegorz et al. [11] investigated the effects of electrolyte concentration on the performance of a PEC cell. They made a two-compartment PEC cell consisting of a CdS photoanode immersed in aqueous sulfide solution, Nafion membrane, platinum cathode, and sulphuric acid solution as the dark-compartment electrolyte. Under their optimized conditions, light to hydrogen conversion efficiency up to 12% was completed under sun light illumination.

A semiconductor is characterized by the energy band gap, E_g. Only that part of incident solar radiation having energy higher than E_g can be absorbed by the semiconductor electrode to generate electron–hole pairs. Accounting for the resistance and other losses, the optimum value of E_g is approximately 2.0 eV [12]. Materials having E_g lower than this value are less effective for splitting water.

In 2006, Kudo [13,14] reported a quantum efficiency of 20% system. Experimentally, Pt-loaded $AgInZn_7S_9$ (E_g = 2.3 eV) immersed in 0.5 M K_2SO_3 showed the highest activity for the H_2 production. The quantum efficiency at 420 nm was 20% using a 300 W Xe lamp, and the rate of H_2 production was 944 μmol/h for 33 cm^2 irradiated area. Its hydrogen volume production rate was 6.41 L/m^2 h.

Wang et al. [15] used a one-step electrodeposition method to produce $AgInS_2$ electrode. They obtained a maximum photocurrent density of 9.28 mA/cm^2 with an applied bias of +1.0 V vs. an Ag/AgCl electrode in contact with electrolyte containing 0.25 M K_2SO_3 and 0.35 M Na_2S. The maximum quantum efficiency was 63% at 560 nm.

Tseng et al. [16] performed a thermodynamic analysis of the PEC hydrogen production for air mass 1.5 (AM 1.5) solar irradiation. The maximum hydrogen production rate and solar-to-hydrogen conversion efficiency under various operation conditions were presented and discussed.

So far, most studies on PEC production of hydrogen have focused on the development of photoelectrode materials. Very little attention has been paid to the reactor design and thermal and transport phenomena analysis. Both Licht's work [8–10] and our previous work [16] were based on thermodynamic consideration only. No discussion on the transport phenomena and reactor design was given. It is the purpose of the present work to theoretically investigate the heat transfer and flow characteristics of PEC reactors and study the effects of several parameters on the temperature of the system, the solar-to-hydrogen efficiency, η_{SH}, and the hydrogen production rate.

2. Analysis

The schematic diagram of the solar hydrogen reactor considered in this work is depicted in Fig. 1. The solar incidence is directly applied to the reactor. The size of the anode is fixed at 100 mm high and 2 mm thick. The front wall of the reactor is a low absorptive glass. A glass wall is also used as the back wall. The thickness of the back glass wall is designated as G. To hold more thermal energy inside the reactor, an insulation layer of thickness A is used in some cases. The anode is made of fluorine-doped tin oxide (FTO) glass coated with semiconductor films such as Fe_2O_3 or TiO_2. Four designs are studied in this work. Design A: G = 5 mm and A = 0 mm; Design B: G = 5 mm and A = 0 mm, the outside face of the glass is coated opaque; Design C: G = 0 mm and A = 20 mm (thermal conductivity k_A = 0.05 W/m K); Design D: G = 5 mm and A = 20 mm. The spectral solar radiation (AM 1.5) [17] and the measured spectral absorption coefficients of the FTO and glass are shown in Fig. 2. These values are used in the

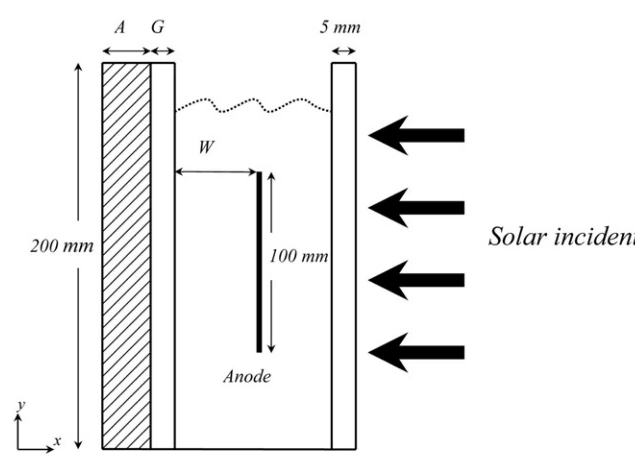

Fig. 1 – The schematic diagram of solar hydrogen reactor. A: thickness of insulator, G: thickness of glass, W: distance between the anode and the glass wall.

numerical simulation. Although electrolytes such as potassium hydroxide solution (KOH) are often used in a practical reactor, water is considered in this study for its availability of optical and thermal properties [18–20].

Steady state, laminar, incompressible and Newtonian flow is considered, and the Boussinesq approximation is employed in this work. The governing equations for this system can be expressed as:

Continuity equation:

$$\frac{\partial(\rho u)}{\partial x}+\frac{\partial(\rho v)}{\partial y}=0 \tag{5}$$

x-momentum equation:

$$u\frac{\partial(\rho u)}{\partial x}+v\frac{\partial(\rho u)}{\partial y}=-\frac{\partial p}{\partial x}+\mu\left(\frac{\partial^2 u}{\partial x^2}+\frac{\partial^2 u}{\partial y^2}\right) \tag{6}$$

y-momentum equation:

$$u\frac{\partial(\rho v)}{\partial x}+v\frac{\partial(\rho v)}{\partial y}=-\frac{\partial p}{\partial y}+\mu\left(\frac{\partial^2 v}{\partial x^2}+\frac{\partial^2 v}{\partial y^2}\right)-\rho g\beta(T-T_0) \tag{7}$$

Energy equation:

$$u\frac{\partial(\rho c_p T)}{\partial x}+v\frac{\partial(\rho c_p T)}{\partial y}=k\left(\frac{\partial^2 T}{\partial x^2}+\frac{\partial^2 T}{\partial y^2}\right)-\nabla\cdot q^r \tag{8}$$

The radiative transfer equation (RTE) [21]:

$$\frac{dI_\lambda}{ds}=\alpha_\lambda I_{b\lambda}(T)-\alpha_\lambda I_\lambda \tag{9}$$

$$\nabla\cdot q^r=\int_0^\infty \alpha_\lambda\left(4\pi I_{b\lambda}-\int_{4\pi} I_\lambda d\Omega\right)d\lambda \tag{10}$$

where $I_{b\lambda}$ is the black body intensity. The effect of scattering is not considered in this work.

Except the bottom wall, which is assumed adiabatic, the heat transfer between the reactor and the surroundings is considered in the work. Computational domain is extended 1.5 times the height of the reactor in the lateral and upward directions so that interactions between the reactor and the surroundings can be simulated. The SIMPLEC algorithm [22] is employed in this work. Commercial CFD software package, FLUENT 6.3, is used as the numerical tool in this study. This software solves the Navier–Stokes equations using an unstructured finite-volume method and the RTE using the discrete ordinates method [23,24]. Some numerical techniques are used through the user-defined function (UDF).

Based on the AM 1.5, the fraction of solar energy that is available for water splitting is integrated over the wavelength as a function of E_g, as shown in Fig. 2. The percentage of short wave energy is 61.6% for $E_g = 1.5$ eV, 36.7% for $E_g = 2.0$ eV, 18.0% for $E_g = 2.5$ eV, and 6.15% for $E_g = 3.0$ eV. Properties of water used in the calculation such as density, heat capacity, thermal conductivity, viscosity and thermal expansion coefficient are functions of temperature. Some modelling techniques [25–29] are used in this work.

The spectral absorption coefficient of water, FTO and glass are averaged for the short and long wave regions respectively using:

$$\alpha_{ave}=\frac{\int_{\lambda_1}^{\lambda_2}\alpha_\lambda E_\lambda d\lambda}{\int_0^\infty E_\lambda d\lambda} \tag{11}$$

3. Results and discussion

The solar incidence is divided into short and long wavelength parts according to E_g of the photoelectrode. The short wavelength part is directed to the photoanode for the generation of electro-hole pairs, and the long wavelength part is used for

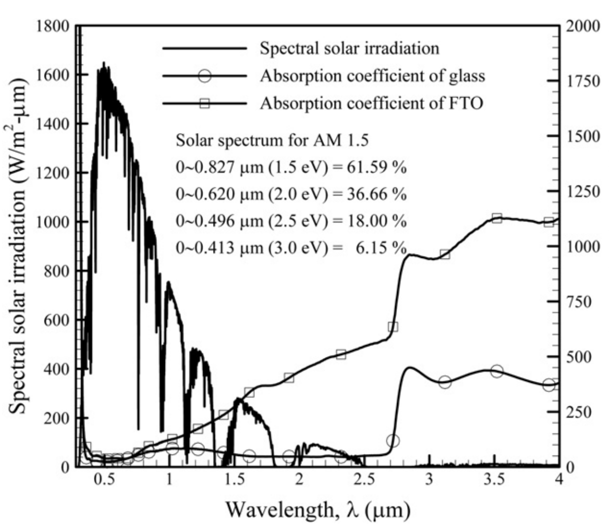

Fig. 2 – The spectral solar irradiation and the absorption coefficient of glass and FTO.

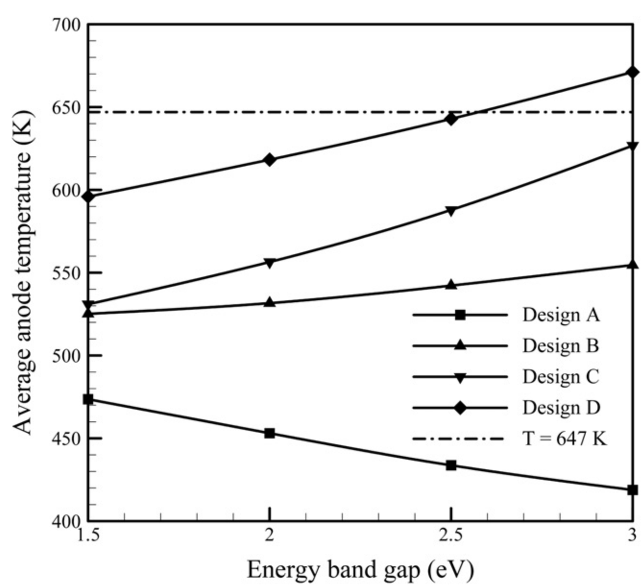

Fig. 3 – Average anode temperature for the four different reactor designs with W = 10 mm, solar incident flux = 4000 W/m^2 and QE = 30%. (1)Design A: G = 5 mm and A = 0 mm; (2) Design B: G = 5 mm and A = 0 mm, the outside face of glass is coated opaque; (3) Design C: G = 0 mm and A = 20 mm (k_A = 0.05 W/m K); (4) Design D: G = 5 mm and A = 20 mm.

heating the electrolyte. Four energy band gaps, 1.5 eV, 2.0 eV, 2.5 eV, and 3.0 eV are considered as examples in this work. Representative numerical results of hydrogen volume production rate and η_{SH} will be presented and discussed. Because the design of PEC reactors has rarely been studied previously, the attention of this work will be given to the effects of the reactor design. Effects of the solar irradiation, glass thickness G, the distance between the anode and glass wall W and the quantum efficiency QE will also be investigated. The insulator used as an example is the rock wool, with a thermal conductivity of 0.05 W/m K. A is fixed at 20 mm. To prevent the water from boiling, the operating pressure is varied according to the maximum temperature inside the reactor.

3.1. *Effects of reactor design*

Fig. 3 shows the average anode temperature versus E_g of the photoelectrode for the four reactor designs with W = 10 mm and solar incident flux = 4000 W/m^2 (concentration ratio of 4). The average anode temperature of design A decreases as E_g increases. On the contrary, the average anode temperature of designs B, C and D increases as E_g increases. For design A, the left wall is semi-transparent to the long wave energy, so portions of the solar irradiation go through the water, the glass wall, and then escape to the outside. As E_g is increased, less energy is used for the generation of electro-hole pairs, and more energy is lost to the outside through the long wavelength part. Therefore, the average anode temperature decreases. On the other hand, for designs B, C, and D, the left wall is made opaque either by the insulation or coating. Therefore, very few radiant energy is lost to the outside. As E_g is increased, more energy is used for heating, and hence higher average anode temperature.

Since the long wavelength energy is used for heating the reactor, it is an essential subject to keep as much long wavelength energy inside the reactor as possible. The best among the four is design D. It has an opaque insulator to cut both conduction and radiation losses, while the left glass wall acts as a long wavelength energy storage due to its good absorptivity in that wavelength region. For solar incident flux of 4000 W/m^2 and quantum efficiency QE of 30%, the average anode temperature is 623 K and 686 K respectively for Fe_2O_3 (E_g = 2.1 eV) and TiO_2 (E_g = 3.2 eV) in design D. But with design A, the average anode temperature is only 449 K and 411 K respectively for Fe_2O_3 and TiO_2.

Fig. 4 shows the reactor temperature distributions for designs A, B, C and D with anodes of different E_g for solar incident flux = 4000 W/m^2 and QE = 30%. In the PEC reactor, the short wavelength energy is directed to the photoanode for splitting water. QE = 30% means the remaining 70% of

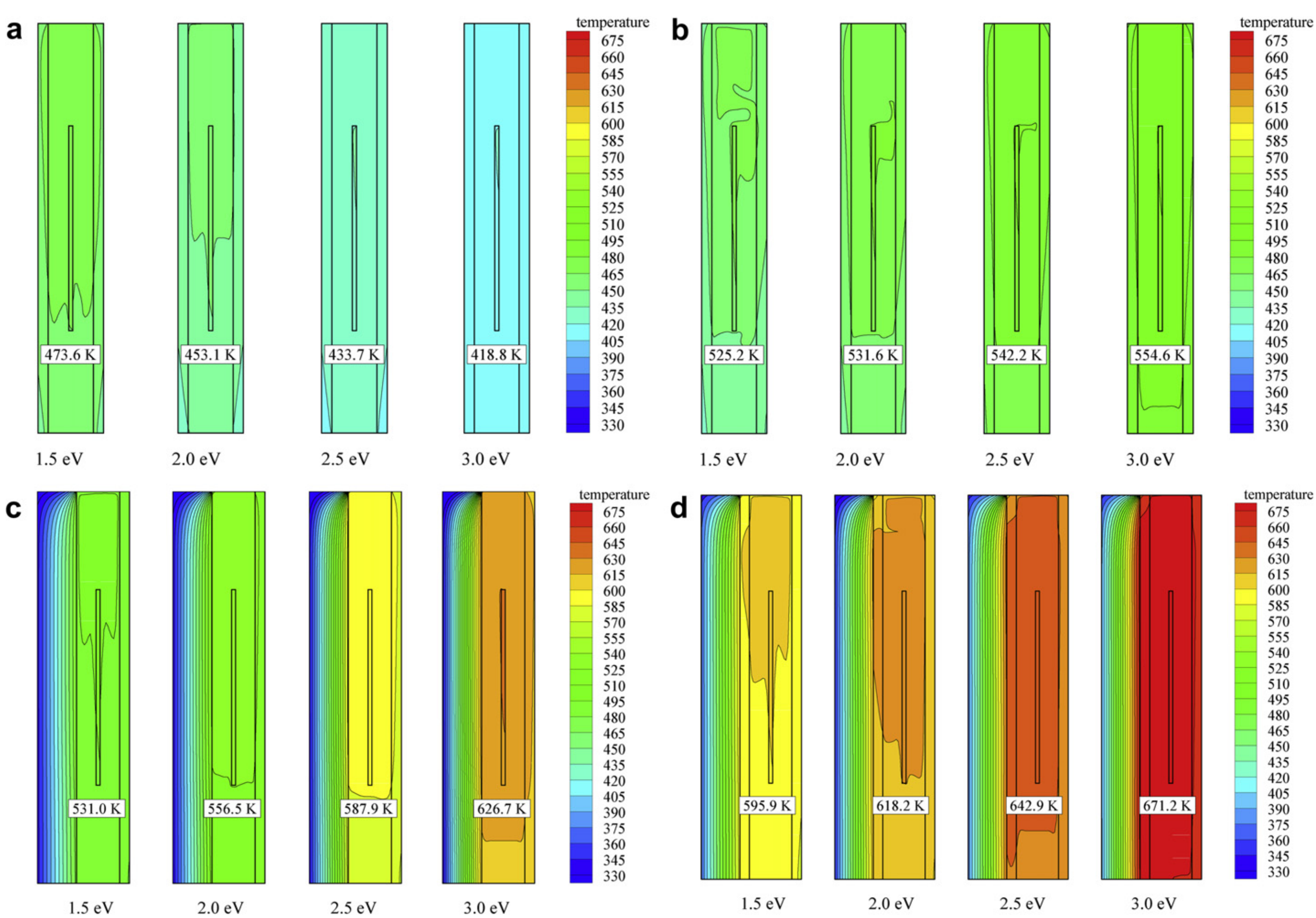

Fig. 4 – Temperature distributions for the four different reactor designs with anodes of different E_g, W = 10 mm, solar incident flux = 4000 W/m^2 and QE = 30%.

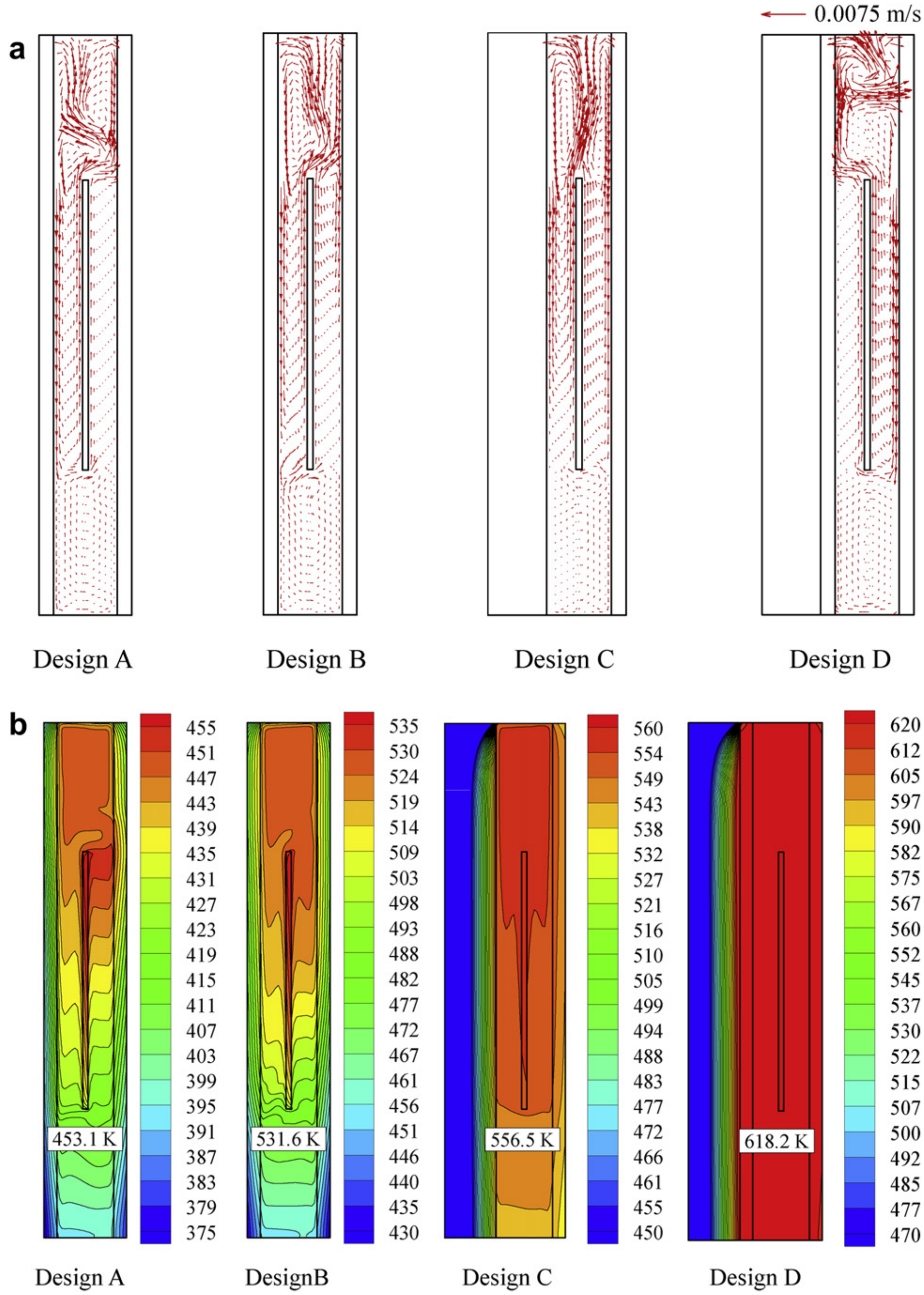

Fig. 5 – The flow and thermal characteristics of the four different reactor designs for E_g = 2.0 eV, solar incident flux = 4000 W/m^2 and QE = 30%, (a) velocity vector; (b) temperature distribution.

absorbed short wavelength energy is converted to heat. As E_g increases, this converted thermal energy decreases. Because in design A, much of the long wavelength energy is lost to the outside, the converted thermal energy in the short wavelength part plays more important role than in other designs. For design A, the average anode temperature is 474 K, 453 K, 434 K and 419 K respectively for $E_g = 1.5$ eV, 2.0 eV, 2.5 eV and 3.0 eV.

In design B, the outside face of the left glass wall is coated opaque to prevent the loss of long wavelength radiant energy through the glass. The average anode temperature increases slightly as E_g is increased. For design B, the average anode temperature is found to be 525 K, 532 K, 542 K and 555 K respectively for $E_g = 1.5$ eV, 2.0 eV, 2.5 eV and 3.0 eV.

In design C, compared with design B, the left glass wall is replaced by a 20 mm thick insulator (k_A = 0.05 W/m K) to further cut the heat loss to the outside by radiation and conduction. As a result, the energy remained inside the reactor is higher than that in design B. For design C, the average anode temperature is 531 K, 557 K, 588 K and 627 K respectively for $E_g = 1.5$ eV, 2.0 eV, 2.5 eV and 3.0 eV.

In design D, compared with design C, a 5 mm thick glass is placed inside the insulator to absorb the long wavelength energy. For $E_g = 1.5$ eV, about 85% of the long wavelength energy is absorbed by the glass wall. The absorbed energy raises the temperature of the glass, and re-emits to heat the water and electrode. As E_g is increased, more long wavelength energy is available for heating the reactor. The average anode temperature is 596 K, 618 K, 643 K and 671 K for $E_g = 1.5$ eV, 2.0 eV, 2.5 eV and 3.0 eV, respectively.

Fig. 5(a) and (b) presents the flow and thermal characteristics of the four different reactor designs for $E_g = 2.0$ eV, solar incident flux = 4000 W/m^2 and $QE = 30\%$. The photoanode has the highest temperature due to the absorption of solar irradiation.

Comparing with the other three designs, design A has the lowest temperature because most of the long wavelength energy is lost to the outside. The fluids in the two channels separated by the anode have different velocities. The right-hand-side channel (channel R) has smaller velocity due to more pronounced thermally stratified phenomenon. The fluid therefore flows to the right when it passes the top of the anode plate. The flow in design B is similar. However, the velocity in channel R is higher than that in design A due to lesser extent of thermal stratification. The distortion of the flow pattern is not as severe.

For design C, a thermal insulation layer is used, and the temperature inside the reactor is increased and distributed more uniformly. The flow velocities near both sides of the anode plate are almost the same, and two nearly symmetric circulations form in the top region.

For design D, the reactor temperature is further increased. The temperature on the right surface of the anode is slightly higher than that on the left surface due to direct irradiation of solar flux. Therefore, the velocity in the right channel is higher than that in the left channel, and the flow turns to the left as it passes the top of the anode plate.

Fig. 6 shows η_{SH} for the four designs. η_{SH} is defined as

$$\eta_{SH} = \frac{QE \times E_s \times \Delta H_{H_2}(298\ \text{K}, 1\ \text{bar}) / \Delta G_{H_2O}(T, p)}{E_{in}} \tag{12}$$

where E_s is the energy higher than E_g, and E_{in} is the total incident solar energy. ΔH_{H_2} is the heating value of H_2 at the standard state and ΔG_{H_2O} is the Gibbs free energy of water dissociation reaction at reactor temperature and pressure.

For solar incident flux of 4000 W/m^2 and QE of 30%, η_{SH} is 14.1% and 2.6% respectively for Fe_2O_3 and TiO_2 with design D, and 12.7% and 2.2% with design A. Comparing designs A and D, the enhancement of η_{SH} is respectively 11% and 18% for Fe_2O_3 and TiO_2.

3.2. Effects of solar incident flux

To study the effects on the hydrogen volume product rate and solar-to-hydrogen efficiency, the solar incident flux is assumed to be 1000 W/m^2 for the unconcentrated case, and 2000 W/m^2, 3000 W/m^2 and 4000 W/m^2 for the cases using a solar concentrator. The average anode temperatures under different solar incident flux versus E_g with $W = 10$ mm, $G = 10$ mm and $QE = 30\%$ for design D are shown in Fig. 7. As expected, as solar incident flux increases, the average anode temperature increases. For solar incident flux = 4000 W/m^2, the average anode temperature is close to 647 K.

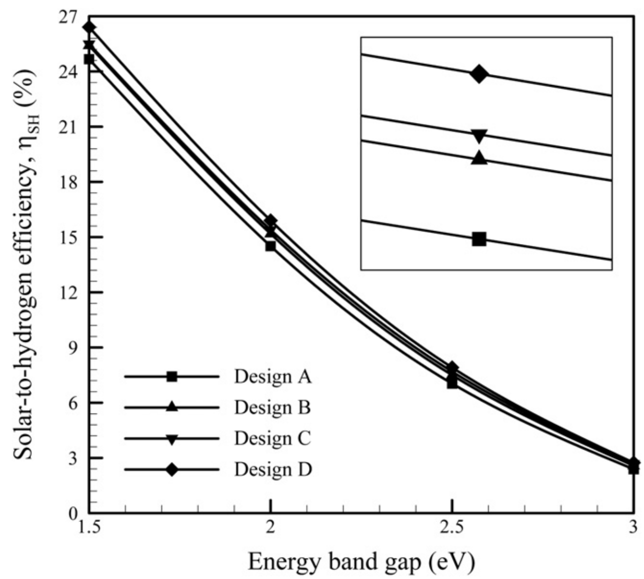

Fig. 6 – Solar-to-hydrogen efficiency for the four different reactor designs with W = 10 mm, solar incident flux = 4000 W/m^2 and QE = 30%.

Fig. 8 depicts the hydrogen volume production rate for different solar incident flux. The hydrogen volume production rate is calculated from the following equation

$$\phi = \frac{QE \times E_s}{\Delta G_{H_2O}(T, p)} \times 3600\ \text{s} \times 22.4\ \text{L} \tag{13}$$

At the standard state, the gas volume of 1 mol is 22.4 L.

Because the energy available for splitting water decreases as E_g is increased, the hydrogen production rate decreases. For solar incident flux = 1000 W/m^2 and $QE = 30\%$ with design D, the hydrogen volume production rate is 35.0 L/m^2 h and 5.7 L/m^2 h respectively for Fe_2O_3 and TiO_2. If solar incident flux is raised to

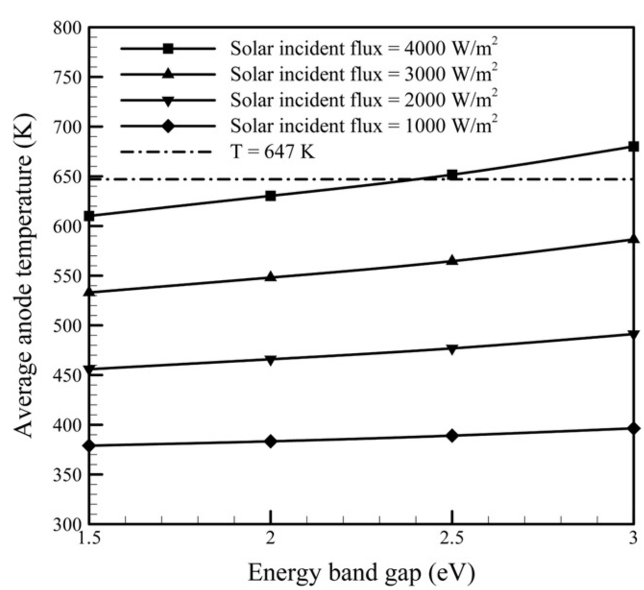

Fig. 7 – Average anode temperature for different solar incident flux in design D with W = 10 mm, G = 10 mm, A = 20 mm and QE = 30%.

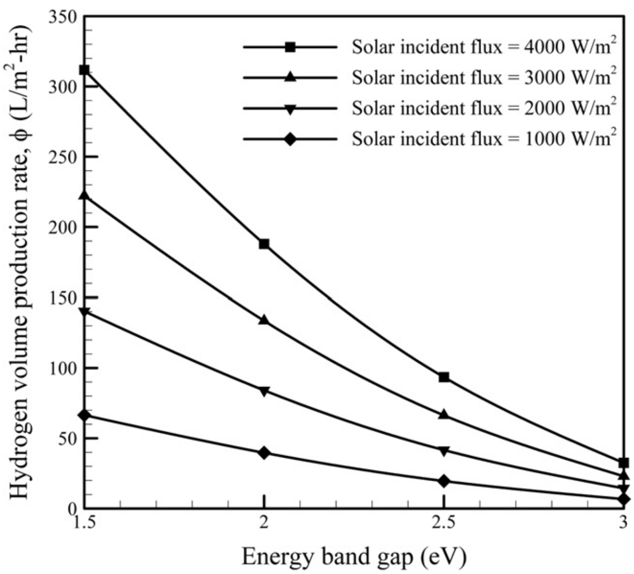

Fig. 8 – Hydrogen volume production rate for different solar incident flux with W = 10 mm, G = 10 mm, A = 20 mm and QE = 30%.

4000 W/m^2 while keeping other parameters unchanged, the hydrogen volume production rate is increased to 166 L/m^2 h and 31.5 L/m^2 h for Fe_2O_3 and TiO_2 respectively. Therefore, increasing solar incident flux is an effective way to raise the hydrogen volume production rate.

Fig. 9 presents the effect of solar incident flux on η_{SH}. As solar incident flux is increased, the average anode temperature is increased. Therefore, the energy required for splitting water is decreased. For a solar incident flux of 1000 W/m^2 and QE = 30% with design D, η_{SH} is 12.3% and 2.3% respectively for Fe_2O_3 and TiO_2. If the solar incident flux is raised to 4000 W/m^2, η_{SH} is increased to 14.1% and 2.6% for Fe_2O_3 and TiO_2 respectively. The enhancement is 14.6% and 13.0% respectively for Fe_2O_3 and TiO_2 as solar incident flux is increased from 1000 W/m^2 to 4000 W/m^2 with design D.

3.3. *Effects of G and W*

Figs. 10 and 11 show the effects of the back glass thickness G and the distance between anode and the glass wall W for design D with solar incident flux = 4000 W/m^2 and QE = 30%. As shown in Fig. 10, the average anode temperature increases with increasing G and decreases with increasing W. For the case of E_g = 1.5 eV, α_{ave} = 381.5 1/m in the long wavelength region, and the absorptivity of the glass is 32%, 85% and 98% respectively for G = 1 mm, 5 mm and 10 mm. This means that as G is increased, more long wavelength energy is absorbed by the glass. This absorbed energy is re-emitted to heat the water. On the other hand, as W is increased, more water exists in the reactor. The absorbed solar energy is dispersed into larger amount of water, and the average anode temperature decreases. Therefore, larger G and smaller W are good for heating the reactor.

In Fig. 11, the variation of η_{SH} with G and W is depicted. For G = 10 mm and W = 10 mm, η_{SH} is 14.1% and 2.7% respectively for Fe_2O_3 and TiO_2. But for G = 1 mm and W = 100 mm, η_{SH} is 13.0% and 2.4% respectively for Fe_2O_3 and TiO_2. The enhancement using the former design parameters over the latter ones is 8.5% and 12.5% for Fe_2O_3 and TiO_2, respectively.

3.4. *Effects of quantum efficiency*

Fig. 12 shows the effects of QE on the average anode temperature for solar incident flux = 4000 W/m^2 with design D. As explained previously, the average anode temperature increases as E_g is increased. Increasing QE, the average anode temperature decreases due to more short wavelength energy

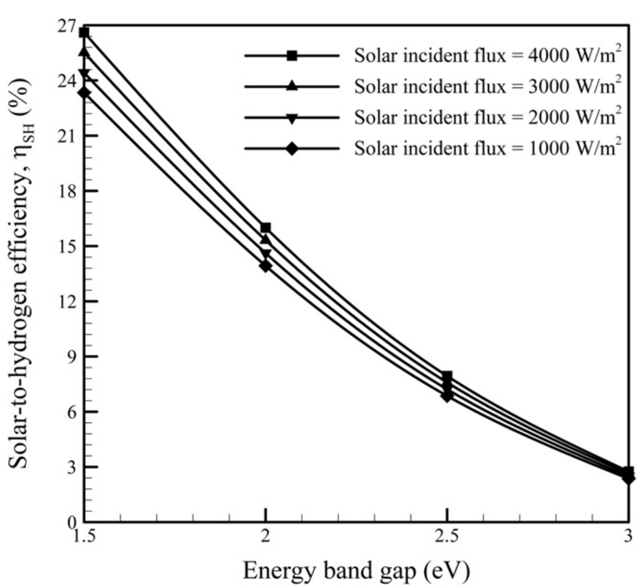

Fig. 9 – Solar-to-hydrogen efficiency for different solar incident flux with W = 10 mm, G = 10 mm, A = 20 mm and QE = 30%.

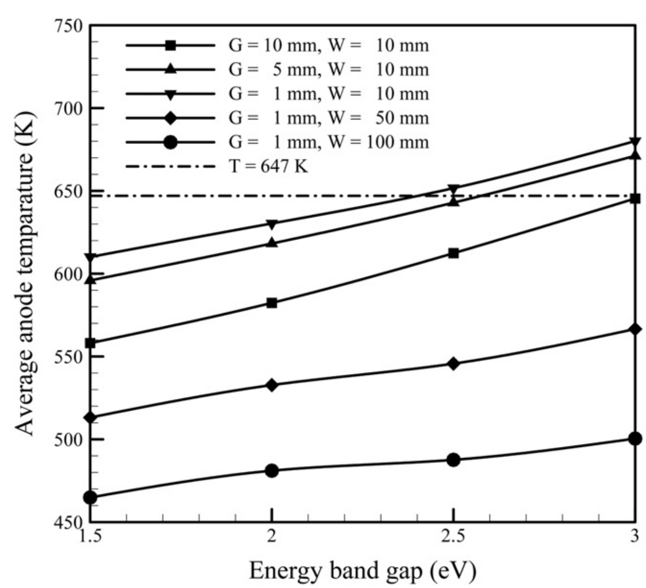

Fig. 10 – Average anode temperature for different G and W with A = 20 mm, solar incident flux = 4000 W/m^2 and QE = 30%.

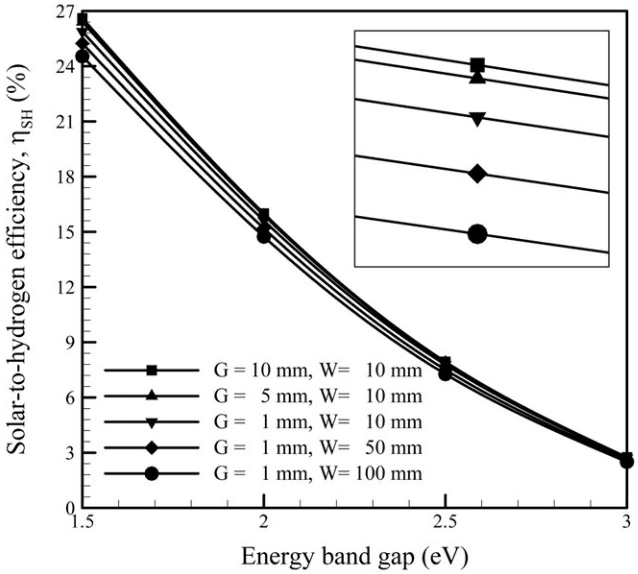

Fig. 11 – Solar-to-hydrogen efficiency for different G and W with A = 20 mm, solar incident flux = 4000 W/m^2 and QE = 30%.

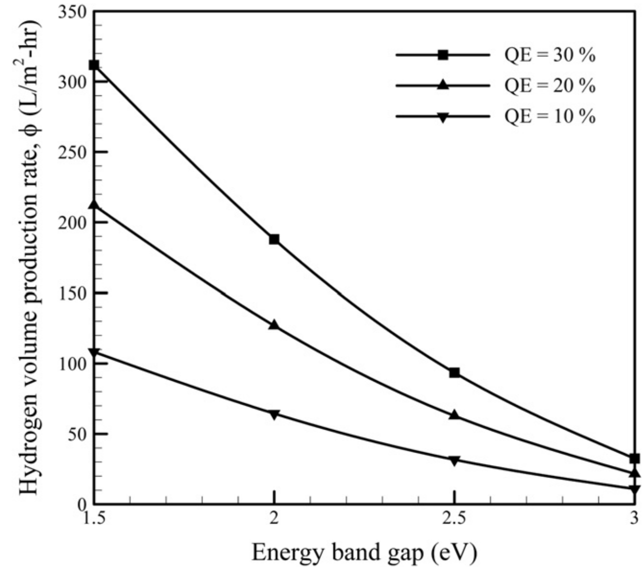

Fig. 13 – Hydrogen volume production rate for different QE with W = 10 mm, G = 10 mm, A = 20 mm and solar incident flux = 4000 W/m^2.

being used to produce electron–hole pairs and less short wavelength energy remained to be converted into heat. The remaining short wavelength energy is larger for lower E_g. Therefore, the difference in anode temperature caused by QE is more obvious for lower E_g.

Figs. 13 and 14 show the effects of QE on the hydrogen volume production rate and η_{SH} for solar incident flux of 4000 W/m^2. For TiO_2, the hydrogen volume production rate is 9.8 L/m^2 h, 20.7 L/m^2 h and 31.5 L/m^2 h respectively for QE = 10%, 20% and 30%. For Fe_2O_3, the hydrogen volume production rate is 56.8 L/m^2 h, 112 L/m^2 h and 166 L/m^2 h respectively for QE = 10%, 20% and 30%. Furthermore, for TiO_2, η_{SH} is 0.9%, 1.7% and 2.6% respectively for QE = 10%, 20% and 30%, and for Fe_2O_3, η_{SH} is 4.8%, 9.5% and 14.1% respectively for QE = 10%, 20% and 30%. As a comparison, Kudo [13,14] used Pt-loaded $AgInZn_7S_9$ (E_g = 2.3 eV) as the photoanode, and experimentally measured the H_2 production rate under a 300 W Xe lamp. The rate of H_2 production was 944 μmol/h at 33 cm^2 (equivalent to 6.41 L/h m^2) and the quantum efficiency at 420 nm was 20%. Using desing D of the present study with QE = 20% and a 300 W visual light incidence, the hydrogen volume production rate is 7.10 L/h m^2. The result is very close to Kudo's result.

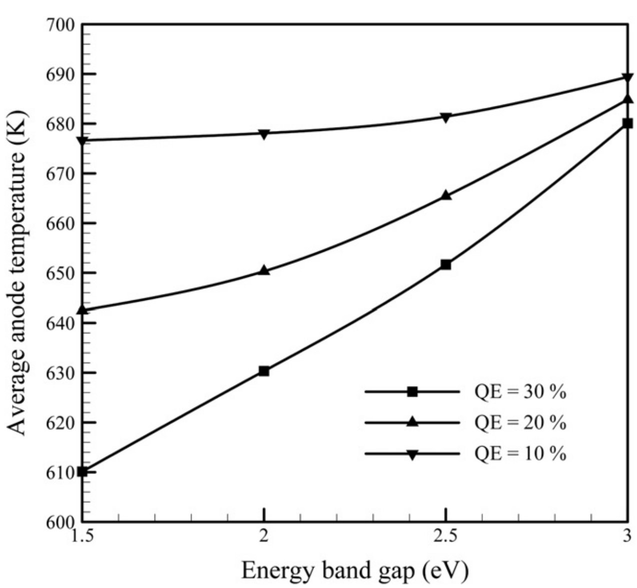

Fig. 12 – Average anode temperature for different QE with W = 10 mm, G = 10 mm, A = 20 mm and solar incident flux = 4000 W/m^2.

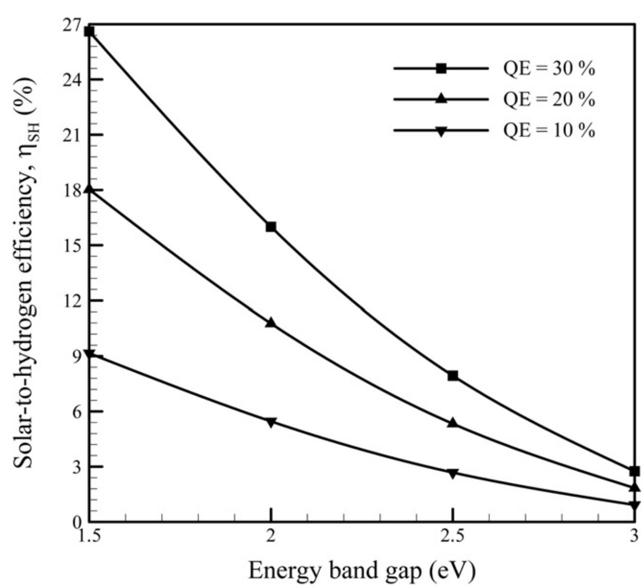

Fig. 14 – Solar-to-hydrogen efficiency for different QE with W = 10 mm, G = 10 mm, A = 20 mm and solar incident flux = 4000 W/m^2.

4. Conclusions

The heat transfer and flow characteristics of PEC hydrogen reactors have been investigated numerically. Four different reactor designs are studied in this work. Solar irradiation is separated spectrally into short and long wavelength parts depending on the energy band gap of the photoelectrode used. Effects of several parameters on the hydrogen volume production rate and solar-to-hydrogen efficiency are studied.

Of the four designs, design D has the best efficiency because the long wavelength energy is used effectively. Comparing with design A, the enhancement in η_{SH} of design D for solar incident flux = 4000 W/m^2 and $QE = 30\%$ is 11.0% and 18.2% respectively for Fe_2O_3 and TiO_2.

As the solar incident flux is increased from 1000 W/m^2 to 4000 W/m^2, for Fe_2O_3 with $QE = 30\%$ and design D, the hydrogen volume production rate is increased from 35.0 L/m^2 h to 166/m^2 h and the enhancement in η_{SH} is 14.6%.

Larger G and smaller W are good for heating the reactor. As G is increased from 1 mm to 10 mm and W is decreased from 100 mm to 10 mm, for Fe_2O_3 with solar incident flux = 4000 W/m^2, $QE = 30\%$ and design D, the enhancement in η_{SH} is 8.5% and 12.5%, respectively.

QE directly affects the hydrogen volume production rate and η_{SH}. As QE is increased, both hydrogen volume production rate and η_{SH} are increased.

Acknowledgements

This work was partially supported by the National Science Council of Taiwan through the grant no. NSC 99-3113-P-008-003. The authors would also like to express their thankfulness to the reviewers for their helpful comments.

REFERENCES

[1] Fujishima A, Honda K. Electrochemical photolysis of water at a semiconductor electrode. Nature 1972;238:37–8.
[2] Khaselev O, Bansal A, Turner JA. High-effiency integrated multijunction photovoltaic/electrolysis systems for hydrogen production. Int J Hydrogen Energy 2001;26:127–32.
[3] Murphy AB, Barnes PRF, Randeniya LK, Plumb IC, Grey IE, Horne MD, et al. Efficiency of solar water splitting using semiconductor electrodes. Int J Hydrogen Energy 2006;31:1999–2017.
[4] Peharz G, Dimroth F, Wittstadt U. Solar hydrogen production by water splitting with a conversion efficiency of 18%. Int J Hydrogen Energy 2007;32:3248–52.
[5] Shaban YA, Khan SUM. Visible light active carbon modified n-TiO_2 for efficient hydrogen production by photoelectrochemical splitting of water. Int J Hydrogen Energy 2008;33:1118–26.
[6] Bak T, Nowotny J, Rekas M, Sorrell CC. Photo-electrochemical properties of the TiO_2-Pt system in aqueous solutions. Int J Hydrogen Energy 2002;27:19–26.
[7] Momirlan M, Veziroglu TN. Current status of hydrogen energy. Renew Sustain Energ Rev 2002;6:141–79.
[8] Licht S. Efficient solar generation of hydrogen fuel – a fundamental analysis. Electrochem Commun 2002;4:790–5.
[9] Licht S. Solar water splitting to generate hydrogen fuel: photothermal electrochemical analysis. J Phys Chem B 2003;107:4253–60.
[10] Licht S. Solar water splitting to generate hydrogen fuel: a photothermal electrochemical analysis. Int J Hydrogen Energy 2005;30:459–70.
[11] Grzegorz M, Atsuo K, Sergiy M, Araib T, Shinodab K, Tohjib K. Optimization of a two-compartment photoelectrochemical cell. Int J Hydrogen Energy 2003;28:919–26.
[12] Bak T, Nowotny J, Rekas M, Sorrell CC. Photo-electrochemical hydrogen generation from water using solar energy: materials-related aspects. Int J Hydrogen Energy 2002;27:991–1022.
[13] Kudo A. Development of photocatalyst materials for water splitting. Int J Hydrogen Energy 2006;31:197–202.
[14] Kudo A. Recent progress in the development of visible light-driven powdered photocatalysts for water splitting. Int J Hydrogen Energy 2007;32:2673–8.
[15] Wang CH, Cheng KW, Tseng CJ. Photoelectrochemical properties of AgInS2 thin films prepared using electrodeposition. Sol Energ Mater Sol Cell 2011;95:453–61.
[16] Tseng CL, Tseng CJ, Chen JC. Thermodynamic analysis of a photoelectrochemical hydrogen production system. Int J Hydrogen Energy 2010;35:2781–5.
[17] http://rredc.nrel.gov/solar/spectra/am1.5/.
[18] Segelstein DJ. The complex refractive index of water; 1981. Report of University of Missouri-Kansas City.
[19] Chase MW. JANAF thermochemical tables. 3rd ed. New York: American Chemical Society; 1986.
[20] Palik ED. Handbook of optical constants of solids. 1st ed. Orlando: Academic Press; 1985.
[21] Modest MF. Radiative heat transfer. 2nd ed. New York: McGraw-Hill; 2003.
[22] Patankar SV. Numerical heat transfer and fluid flow. 1st ed. Washington: McGraw-Hill; 1980.
[23] Chui EH, Raithby GD. A finite-volume method for predicting a radiant heat transfer in enclosures with participating media. J Heat Transf 1990;112:415–23.
[24] Chui EH, Raithby GD. Computation of radiant heat transfer on a non-orthogonal mesh using the finite-volume method. Numer Heat Tran B 1993;23:269–88.
[25] Rzayeva MP, Salamov OM, Kerimov MK. Modeling to get hydrogen and oxygen by solar water electrolysis. Int J Hydrogen Energy 2001;26:195–201.
[26] Shukla PK, Karn RK, Singh AK, Srivastava ON. Studies on PV assisted PEC solar cells for hydrogen production through photoelectrolysis of water. Int J Hydrogen Energy 2002;27:135–41.
[27] Kelly NA, Gibson TL. Design and characterization of a robust photoelectrochemical device to generate hydrogen using solar water splitting. Int J Hydrogen Energy 2006;31:1658–73.
[28] Aroutiounian VM, Arakelyan VM, Shahnazaryan GE. Metal oxide photoelectrodes for hydrogen generation using solar radiation-driven water splitting. Solar Energy 2005;78:581–92.
[29] Bolton JR. Solar photo production of hydrogen: a review. Solar Energy 1996;57:37–50.